Journal of Materiomics 11 (2025) 100969

Contents lists available at ScienceDirect

Journal of Materiomics

journal homepage: www.journals.elsevier.com/journal-of-materiomics/

Research paper

Dual-site engineering of N vacancies and K single-atoms in C_3N_4: Enabling spatial charge transfer channels for photocatalysis

Xiao Xu [a, 1], Yao Xiao [a, 1], Xuelian Xu [a], Sónia A.C. Carabineiro [b], Junjiang Zhu [a, *]

[a] Hubei Key Laboratory of Biomass Fibers and Eco-dyeing & Finishing, School of Chemistry and Chemical Engineering, Wuhan Textile University, Wuhan, 430200, China

[b] LAQV-REQUIMTE, Department of Chemistry, NOVA School of Science and Technology, Universidade NOVA de Lisboa, Largo da Torre, 2829-516, Caparica, Portugal

ARTICLE INFO

Article history:
Received 22 August 2024
Received in revised form
3 October 2024
Accepted 7 October 2024
Available online 17 November 2024

Keywords:
C_3N_4
N vacancies
K single-atom
Spatial separation of electrons
Photocatalysis

ABSTRACT

Graphitic carbon nitride (C_3N_4) is a promising photocatalyst due to its suitable band gap and polymer properties, but its efficiency is limited by the poor separation of photoinduced electron/hole (e^-/h^+) pairs. To address this issue, we propose creating N vacancies within the layers and bridging K single-atoms between the C_3N_4 layers through the self-assembly of potassium citrate and melamine–urea monomers. The introduction of N vacancies disrupts the symmetry of C_3N_4, promoting electron transfer along the delocalized π-conjugated network, while the presence of K atoms provides channels for electron transfer between the layers by forming N–K–N bridges, thereby leading to significant enhancement in the separation and transfer of e^-/h^+ pairs across spatial dimension. As expected, the co-modified C_3N_4, with N vacancies and K single-atoms (designated as CN-K-V_N), exhibits excellent photocatalytic performance, with reaction rate constant of 9.69×10^{-2} min^{-1} (7.39×10^{-2} min^{-1} in real water environment) for tetracycline, achieving 80% degradation of tetracycline within 20 min. The reaction mechanism, as well as the toxicity of the degradation intermediates, is deeply discussed. This study provides a strategy to enhance the spatial separation of electrons for photocatalyst, highlighting its significance role in photocatalysis.

1. Introduction

The prevalent presence of antibiotics in aquatic ecosystems has raised environmental concerns due to the potential development of antibiotic-resistant bacteria [1,2]. Tetracycline (TC), a commonly used antibiotic in agriculture and aquaculture, frequently enters water bodies through runoff and improper waste disposal [3]. Its persistence in these environments can disrupt aquatic ecosystems and promote the proliferation of resistant bacteria, posing a serious threat to human health [4,5]. Therefore, it is of critical importance to implement advanced treatment methods to effectively remove TC residues from water sources [6–8].

Photocatalysis has emerged as a promising technology for environmental remediation and pollution control [9–12]. Among potential photocatalysts, graphitic carbon nitride (C_3N_4) stands out due to its straightforward synthesis, responsiveness to visible-light and high stability [13–17]. However, the efficiency of pristine C_3N_4 in photocatalytic applications is significantly hindered by limitations in charge separation and transfer [12,18,19]. Specifically, incomplete polymerization leads to some heptazine rings being interconnected by hydrogen bonds, with the terminal amino groups acting as charge centers, thereby impeding in-plane charge transfer [20]. Additionally, the π-conjugated structure and the weak van der Waals forces between the layers of C_3N_4 hinder interlayer charge transmission [21]. Therefore, enhancing both intralayer and interlayer charge transmission in C_3N_4 is of great significance, yet remains a considerable challenge.

Researchers are actively working to enhance both intralayer and interlayer charge transmission in C_3N_4 [22]. Doping or copolymerization with heteroatoms or functional groups with varying electron affinities and polarities has proved to be highly effective in promoting charge transmission within and between the layers [23–25]. Zhang *et al.* synthesized highly dispersed porous C_3N_4 nanosheets by co-heating with ammonium oxalate monohydrate,

* Corresponding author.
E-mail address: jjzhu@wtu.edu.cn (J. Zhu).
Peer review under responsibility of The Chinese Ceramic Society.
[1] These authors contributed equally to this work.

https://doi.org/10.1016/j.jmat.2024.100969

which improved the integrity of the in-plane heptazine rings. This enhancement increased the electron density of the π-conjugated structure and facilitated intralayer charge transmission [26]. Meanwhile, Mi's team successfully developed K-doped C_3N_4 with high in-plane crystallinity and improved charge transfer capabilities, highlighting the importance of interlayer charge transmission in photocatalytic processes [27]. However, these studies primarily focus on enhancing either interlayer or intralayer charge transmission on C_3N_4 by introducing individual charge transmission channels, with fewer reports exploring the synergistic effects of both mechanisms. Therefore, there is an urgent need for a straightforward approach that can concurrently promote both intralayer and interlayer charge transmission by creating comprehensive charge channels across spatial dimensions.

Doping is an effective way to create defects and single-atom sites that enhance transmission capabilities [28,29]. Numerous studies demonstrate that chemically doped C_3N_4 can significantly improve photocatalytic activity by effectively regulating both interlayer and intralayer charge transmission [30]. Doping can involve atomic substitution, interstitial doping or atomic intercalation, depending on the size and properties of the doped atoms. Non-metallic elements, such as C, O and S, are typically incorporated through atomic substitution due to their lightweight nature, which enhances charge distribution within the intralayer. In contrast, metallic elements, like Na and K, tend to stay in the interlayers due to their large atomic radii, functioning as bridges for electron transmission between the layers [31].

In this work, we prepared N vacancies and K single-atoms co-modified C_3N_4 (CN-K-V_N) through the self-assembly of potassium citrate and melamine−urea monomers, to enhance both intralayer and interlayer charge transmission capabilities. The chemical state and spatial distribution of the N vacancies and K single-atoms were thoroughly investigated using a series of characterizations techniques. Subsequently, theoretical calculations and optoelectronic analyses were employed to examine the electron transmission rates and processes. As expected, N vacancies were introduced into the intralayer, while K single-atoms were incorporated within the interlayers of C_3N_4, effectively accelerating charge separation and transmission across spatial domains. To evaluate the catalytic performance of the materials, we employed the photodegradation of tetracycline hydrochloride (TC) under visible light irradiation as a model reaction. The results demonstrate that the co-modified CN-K-V_N exhibits significantly enhanced catalytic activity, achieving 80% degradation within 20 min, which is 2.6 times higher than the value of pristine C_3N_4. The degradation mechanism is also investigated through *in-situ* diffuse reflectance infrared Fourier transform spectroscopy (DRIFTS) experiments, Liquid Chromatography-Mass Spectrometry (LC-MS) analysis and toxicity assessments. This study reveals a novel approach to design C_3N_4 photocatalysts that incorporate electron transfer in both intra- and inter-layer pathways.

2. Experimental section

2.1. Sample preparation

All chemicals were of analytical grade and used without further purification. The samples were prepared by thermal polymerization. Specifically, 4 g of melamine and 6 g of urea were mixed with 0.0207 g of K_2CO_3 (or alternatively, 0.0210 g of $H_3C_6H_5O_7$ or 0.0324 g of $K_3C_6H_5O_7 \cdot H_2O$) in 20 mL of deionized water. The mixtures were stirred in a water bath at 60 °C until the solvent evaporated, and then dried overnight at the same temperature. The resulting white solids were ground into powder and placed in a covered crucible for heat treatment. The temperature was increased at a rate of 5 °C/min and remained at 550 °C for 4 h. The samples were designated as CN−K, CN-V_N, and CN-K-V_N, respectively, while the sample without adding K or C precursors was labeled as CN.

2.2. Analytical methods

The physical composition of the samples was analyzed by X-ray diffraction (XRD) using a Rigaku Ultima IV diffractometer with Cu K_α radiation, covering a scanning range of 10°−80°. The functional group structure was examined using a Bruker TNESOR-27 Fourier Transform - Infrared Spectrometer (FT-IR) in the range of 400 cm^{-1} to 4000 cm^{-1}. The morphology of the samples was observed by transmission electron microscopy (TEM) with a JEOL JEM-NEOARM microscope. The K content was quantified using inductively coupled plasma atomic emission spectroscopy (ICP-AES, X Series II, Thermo Scientific, Waltham, MA, USA). Brunauer-Emmett-Teller (BET) specific surface area was measured using a Beishide 3H−2000PS2 Surface Area and Pore Size Analyzer, with samples undergoing heat treatment under vacuum at 120 °C for 6 h prior to measurement. The surface chemical composition and chemical states were analyzed by X-ray photoelectron spectrometry (XPS) using a Thermo Scientific K-Alpha spectrometer. The X-ray absorption fine structure spectra at the K-edge were obtained at the BL17B beamline of the National Facility for Protein Science (NFPS), Shanghai Synchrotron Radiation Facility (SSRF). The K L3-edge data were collected at the BL14W beamline of the Shanghai Synchrotron Radiation Facility (SSRF). Ultraviolet−visible - diffuse reflectance spectroscopy (UV−vis DRS) was conducted with a Shimadzu UV-2600i spectrophotometer equipped with an integrating sphere, using $BaSO_4$ as the background, and covering a range of 200−800 nm. The photoluminescence (PL) properties of the samples were measured using a Hitachi F-4700 fluorescence spectrometer with an excitation wavelength of 325 nm. Fluorescence lifetimes were tested using an Edinburgh Instruments FLS 1000 fully modular steady-state transient fluorescence spectrometer under an excitation wavelength of 375 nm. Photocurrent response (PCR) and electrochemical impedance spectroscopy (EIS) were conducted using a CHI 660D electrochemical workstation. Electron paramagnetic resonance (EPR) analysis (MS-5000, Bruker) was employed to detect the generation of photocatalytic products in the system using 5,5-dimethyl-1-pyrroline-N-oxide (DMPO) as a radical spin trapping agent for reactive oxygen species.

2.3. Photocatalytic activity tests

The photocatalytic activity of the catalyst was evaluated by measuring the degradation of TC under simulated sunlight irradiation (wavelengths >420 nm). This simulated sunlight was generated using a 300 W xenon lamp (Microsolar300, Beijing Perfectlight Technology Co., Ltd.) equipped with a 420 nm cut-off filter. Specifically, 50 mg of the catalyst was dispersed into a photocatalytic reaction apparatus containing 50 mL of an aqueous TC solution at a concentration of 20 mg/L. The solution was stirred in the dark for 20 min to establish adsorption-desorption equilibrium. Subsequently, the xenon lamp was turned on for light illumination, with the lamp source positioned 10 cm above the solution surface. Samples were collected every 5 min using a syringe fitted with a 0.45 μm microporous filter membrane. The absorbance of the solution at different time points was measured using a UV−Vis spectrophotometer (TU-1950) at a wavelength of 360 nm. The degradation efficiency of TC was calculated using the formula:

$$\eta\ (\%) = (1 - c_t / c_0) \times 100\%$$

where c_0 is the initial concentration of TC and c_t is the concentration of TC in the aqueous solution at a given time after the reaction.

To evaluate the cycling stability of the catalyst, four consecutive cycling experiments were conducted. The procedures and sampling methods remained consistent with those described above. After each cycle, the spent catalysts were thoroughly rinsed with deionized water, dried in a vacuum oven at 60 °C overnight, and then used for the next run.

2.4. In-situ DRIFTS experiments

To further elucidate the degradation mechanisms of TC, *in-situ* DRIFTS experiments were conducted using solid samples on a FT-IR spectrometer (Thermo Fisher, Nicolet iS50) equipped with a specially designed reaction cell and a liquid nitrogen-cooled HgCdTe (MCT) detector. A mixture consisting of 0.1 g of CN-K-N_V and 0.01 g of TC was finely ground for 15 min and then deposited onto the substrate at the center of the cell. Argon (50 mL/min) was used to purge the cell at 150 °C for 1 h to remove any impurities from the sample surface. After purging, air (30 mL/min) and trace amounts of water vapor were introduced into the reactor, with the infrared signals were collected *in-situ* by the MCT detector.

2.5. Intermediates analysis

The monitoring of intermediate products of TC during the reaction was performed using a High-Performance Liquid Chromatography-Mass Spectrometry (HPLC-MS) system (Shimadzu 2020, Japan). The system was equipped with a VP-ODS C18 column (5 μm, 15.0 × 4.6 mm) and operated at a mobile phase flow rate of 0.2 mL/min at 30 °C. The mobile phase consisted of ultrapure water (containing 0.1% formic acid) as solvent A and acetonitrile as solvent B. A sample injection volume of 20 μL was utilized. MS was conducted in positive-ion mode under the following conditions: capillary voltage of 4 kV, dry heater temperature of 350 °C, nebulizer voltage of 135 V, and N_2 dry gas flow rate of 10 L/min. The MS spectra were recorded within the range of 100 *m*/*z* to 500 *m*/*z*, and the data were analyzed using the qualitative analysis feature of Mass Hunter acquisition software.

2.6. Toxicological calculations

The toxicity of TC and its intermediates was assessed using the quantitative structure–activity relationship (QSAR) method, employing the Toxicity Estimation Software Tool (T.E.S.T.). The aquatic toxicity was assessed by determining the LC50 values for daphnia magna over a period of 48 h and fathead minnow over a period of 96 h. Mammalian toxicity was gauged by calculating the IGC50 values for oral administration in rats. The developmental toxicity and mutagenicity were determined using group contribution methods. These data serve to measure the potential acute hazards that the compound may pose to humans, animals, and the ecological environment.

2.7. Theoretical calculations

Density Functional Theory (DFT) simulations were conducted using the Vienna ab initio simulation package (VASP 5.4.4). The generalized Perdew–Burke–Ernzerhof (PBE) gradient approximation (GGA) method was applied to calculate the exchange–correlation energies. The electronic states were represented using a plane wave basis with an energy cut-off of 520 eV, and core-valence interactions were described using the projector augmented wave (PAW) method. The convergence criterion for the Hellmann–Feynman forces was set to 0.02 eV/Å, and the energy convergence criterion was 10^{-5} eV. A vacuum layer of 15 Å was implemented to isolate the periodic slabs. During the geometry optimization, a K-point mesh of 4 × 4 × 1 and a Gamma-centered K-point grid of 9 × 9 × 1 were used for Brillouin zone sampling. The band gap was calculated using the VASPKIT package along the Gamma-M–K–Gamma path.

3. Results and discussion

3.1. Characterization of samples

The synthesis procedure of the N vacancy and K single-atom co-modified C_3N_4 is illustrated in Fig. 1a. Potassium citrate precursors are carbonized at 550 °C, during which C atoms replace N atoms, creating N vacancies. Simultaneously, K atoms are incorporated into the interlamination of C_3N_4, forming K single-atoms. Similar methods are employed to synthesize C_3N_4 with N vacancies (CN-V_N) and K-bridged C_3N_4 (CN–K) using citric acid and potassium carbonate precursors, respectively. Bulk C_3N_4 (CN) is prepared without the addition of C or K precursors.

All samples exhibit two distinct diffraction peaks at $2\theta = 13.1°$ and 27.6°, corresponding to the (100) and (002) facets of CN, respectively. These peaks reflect the in-plane triazinocyclic conjugated aromatic motifs and graphite-like carbon interlayer stacking of CN, respectively [32], as shown in Fig. 1b. The diffraction peak at 27.6° for CN shifts slightly to a lower angle (27.5°) upon the addition of K atoms in the CN–K and CN-K-V_N samples. This shift indicates an expansion of the layer spacing in the (002) facet, increasing from 0.322 nm to 0.323 nm, due to the incorporation of K atoms into the interlayer of C_3N_4 [31]. The FT-IR spectra confirm the formation of the CN structure, as shown in Fig. 1c. Specifically, the prominent band at 810 cm^{-1} corresponds to the bending vibrational motion of the triazine ring, while the bands in the range of 1200–1600 cm^{-1} are associated with the stretching vibrations of the aromatic heterocyclic ring. Additionally, the broad bands observed between 2900 and 3500 cm^{-1} arise from the stretching vibrations of hydroxyl groups and residual primary and secondary amine groups in the adsorbed water. These findings align well with the characteristic bands of CN reported in literature [33,34]. Notably, the FT-IR spectra of CN–K and CN-K-V_N exhibit signals corresponding to the stretching vibrations of azide groups at approximately 2180 cm^{-1}, indicating the presence of K–N bonds [35].

High-resolution XPS spectra of C 1s reveal three distinct peaks at 288.2, 286.8 eV and 284.8 eV, corresponding to the N–C=N, C–N_3 and C–C bonds, respectively [35], as shown in Fig. 1d. The increased intensity of the C–C bonding suggests that citric acid and/or potassium citrate undergo carbonization during the thermal condensation process, allowing C atoms to integrate into the framework of CN, forming new C–C bonds. Meanwhile, potassium carbonate decomposes into CO_2, preventing it from contributing additional carbon to the framework of CN–K. In the high-resolution K 2p XPS spectra (Fig. S1), a distinct characteristic peak at 293.2 eV is observed in both CN–K and CN-K-V_N, indicating that K atoms, supplied from the potassium citrate or potassium carbonate, are incorporated into the structure of CN [36]. Additionally, the atomic ratios determined from XPS analysis (Table S1) and that elemental analysis (Fig. S2) reveal that the C/N ratio of CN–K is similar to that of pristine CN, while the C/N ratios of CN-V_N and CN-K-V_N are significantly higher. This confirms that citric acid or potassium citrate brings C atoms to the CN framework, whereas the contribution of potassium carbonate is limited due to the decomposition into CO_2. Notably, potassium citrate provides both C and K atoms.

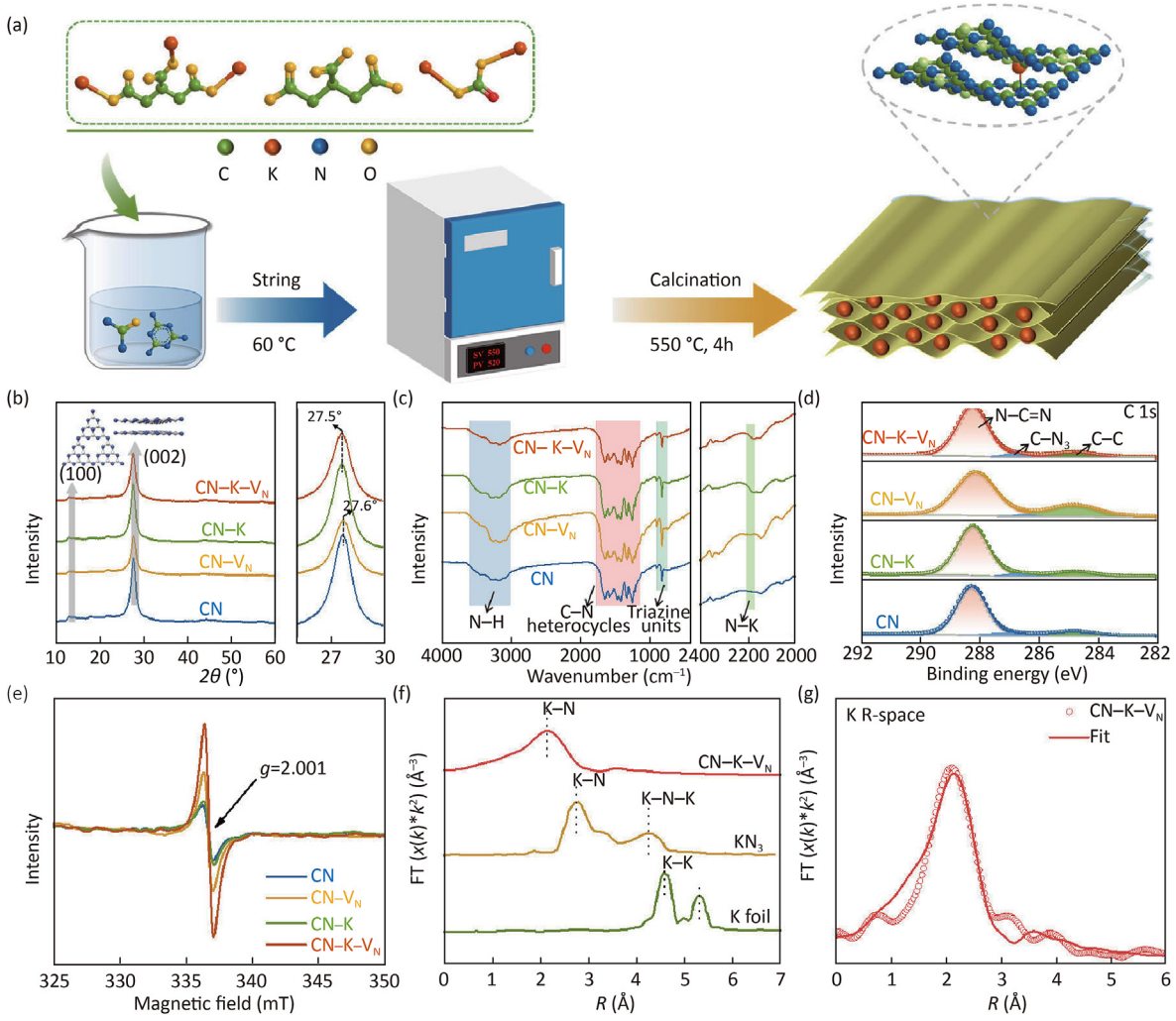

Fig. 1. (a) Schematic illustration of the synthesis process for N vacancies and K single-atom co-modified C_3N_4. Structural and morphological analysis: (b) XRD, (c) FT-IR, (d) high-resolution C 1s XPS, and (e) EPR spectra of the samples. (f) FT-EXAFS results of CN-K-V_N, KN_3 and K foil; (g) χ (R) space spectra fitting curves of K K-edge of CN-K-V_N.

To further illuminate the integration of heteroatoms in C_3N_4, EPR measurements were conducted, as shown in Fig. 1e. All samples display a single Lorentzian line with a g value of 2.001, which is attributed to the delocalized electrons associated with the unpaired electrons in the heptazine unit of carbon [37]. The EPR signals of CN—K exhibit negligible changes compared to those of pristine CN, indicating that the incorporated K atoms hardly contribute to the electronic structure. In contrast, the enhanced EPR signals observed in CN-V_N and CN-K-V_N suggest that the doping of C atoms promotes the formation of N vacancies. This modification optimizes the electronic structure of the heptazine ring, thereby facilitating the delocalization of electrons within the interlayer. The coordination structure of K in CN-K-V_N is further determined using EXELFS analysis. The Fourier-transformed (FT) extended X ray absorption fine structure (EXAFS) curves without phase correction are shown in Fig. 1f. A prominent peak at 2.17 Å is observed in the FT-EXAFS curve for CN-K-V_N (Fig. 1f), which corresponds to K—N scattering path. The K—K peaks at 4.59 Å and 5.32 Å for K foil are absent in CN-K-V_N, thereby confirming the exclusive presence of K single-atoms in CN-K-V_N. Moreover, quantitative structural parameters for K in CN-K-V_N, obtained by least-squares FT-EXAFS fitting (Fig. 1g), indicated five-coordinated K centers with a mean bond length of 2.78 Å (Table S2).

TEM images reveal that CN-K-V_N retains a similarly irregularly curved layered structure but exhibits a more loosely packed arrangement compared to pristine CN, as shown in Fig. 2a and Fig. S3. This loose structure contributes to a large surface area of 61.1 m^2/g (Fig. S4), which enhances the availability of active sites on the surface of CN-K-V_N. Further observations from aberration-corrected HAADF-STEM indicate that K atoms are distributed at atomic scale in CN-K-V_N, as evidenced by numerous intense spots corresponding to K single-atoms (Fig. 2b). In contrast, the K atoms in CN—K, which lacks N vacancies, tend to aggregate, as seen in Fig. S5. This finding suggests that the presence of N vacancies is crucial for the atomic-scale dispersion of K. As-prepared catalysts are analyzed by the inductively coupled plasma atomic emission spectroscopy (ICP-AES), and the K content of CN-K-V_N and CN—K are 5.46% (in mass) and 7.70%, respectively (Table S3). Elemental mappings confirm that the C, N and K are uniformly distributed throughout CN-K-V_N (Fig. 2c). Although the distribution of K atoms appears sparse due to their lower abundance, their presence indicates successful doping into the CN-K-V_N structure. Additionally, zeta potential analysis shows that CN-K-V_N exhibits more negative surface charges than pristine CN (Fig. S6), which can be attributed to the presence of N vacancies and the larger surface area, enabling more basic sites exposed on the surface.

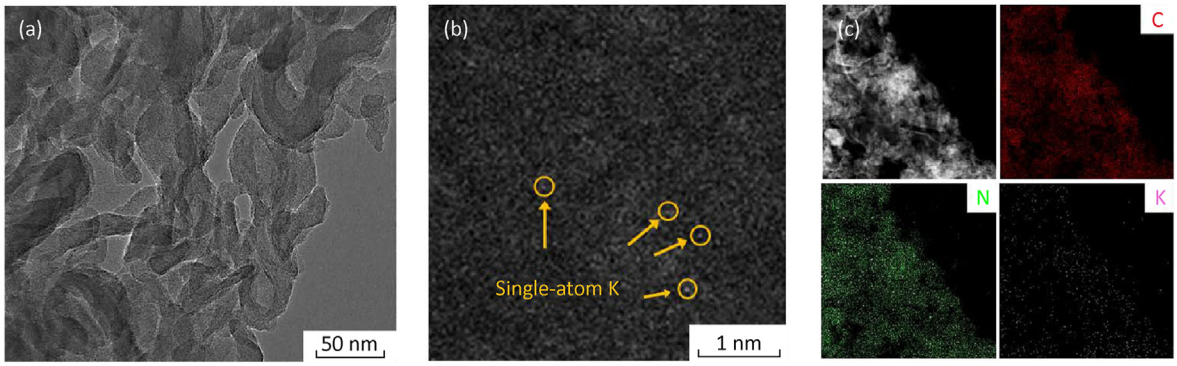

Fig. 2. (a) TEM and (b) HAADF-STEM images, and (c) element mappings of CN-K-V_N.

3.2. DFT calculation analysis

The impact of N vacancies and K single-atoms on the electronic structure of C_3N_4 is investigated through DFT calculations using a two-layer model. Fig. 3a illustrates that the dual-site engineering involving N vacancies and K single-atoms disperses the energy bands, promoting efficient electron transmission across various energy levels compared to CN [35]. Analysis on the Density of States (DOS) plots reveal that N vacancies and K single-atoms induce simultaneous shifts in the C 2p and N 2p orbitals, resulting in an upward shift of the sum of the DOS and a reduction in the band gap (Fig. 3b). Furthermore, an examination of the partial charge density around the K 3p peaks confirms the electronic interaction between K and N atoms in adjacent layers (Fig. 3c). The optimized structure of CN-K-V_N is depicted in Fig. 3d and e, showing that N vacancies are situated within the plane while K atoms are stabilized in the interlayers. The presence of N vacancies creates a non-uniform electron distribution and coordination unsaturation, which facilitates the stabilization of interlayer K ions and the formation of N–K–N bridges for interlayer charge transfer. As a result, N vacancies and K single-atoms establish spatial pathways that enable intraplanar electron localization and interlayer electron shuttling, promoting the rapid separation and migration of photo-generated e^-/h^+ pairs (Fig. 3f).

3.3. Photoelectronic performance analysis

The CN-V_N and CN-K-V_N demonstrate a significant redshift in their light absorption bands compared to CN, while the CN–K shows minimal changes (Fig. 4a). This indicates that the primary factor responsible for broadening the light absorption range is the presence of N vacancies, rather than the K single-atoms. Among the samples, CN-K-V_N exhibits the most pronounced redshift and the highest light absorption intensity, attributed to the dual-site engineering involving both N vacancies and K single-atoms, which modifies both the conduction band (CB) and the valence band (VB) of CN. To further investigate the effects of N vacancies and K single-atoms on charge separation and transmission, we conducted photoelectrochemical measurements, steady-state PL analyses, and time-resolved fluorescence decay spectroscopy. Fig. 4b illustrates the photocurrent responses of CN and CN-K-V_N, showing a significant increase in photocurrent intensity from CN to CN-K-V_N. This finding indicates that electrons in CN-K-V_N can be more readily excited under illumination, which aligns with the UV–visible diffuse emission. Additionally, the EIS plots demonstrate that CN-K-V_N has a smaller radius compared to CN, indicating lower charge

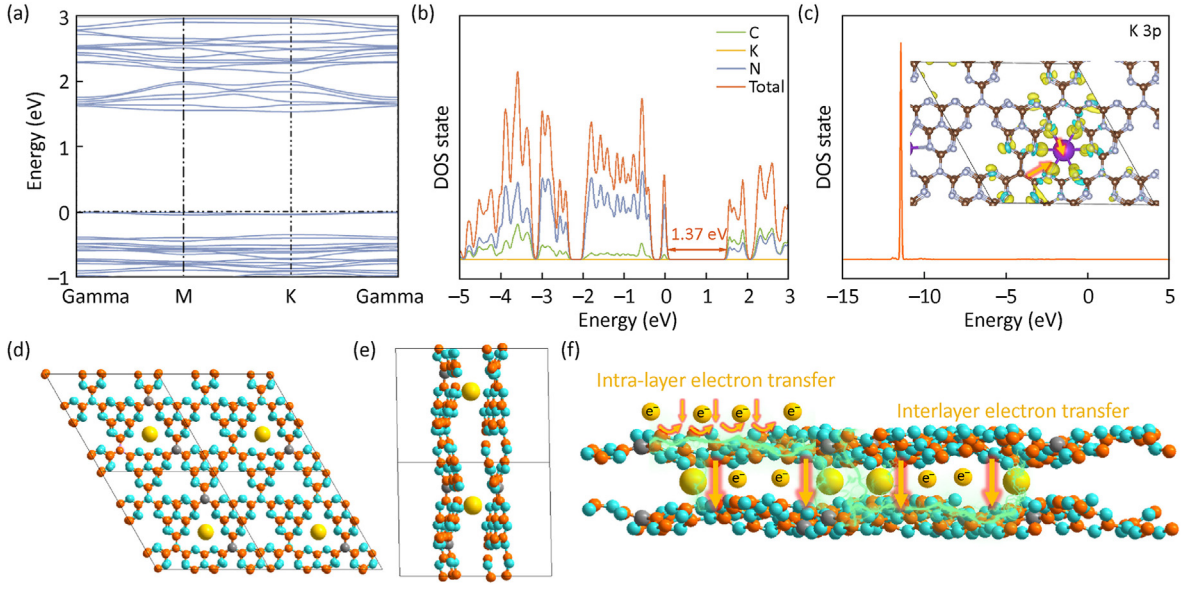

Fig. 3. (a, b) Calculated electronic band structures and DOS plots for CN-K-V_N; (c) Contribution of K atoms to the DOS (Inset: Partial charge density around the K 3p orbitals in CN-K-V_N); (d) Top view and (e) side view of the CN-K-V_N structure; (f) Schematic representation of spatial charge transfer pathways in CN-K-V_N.

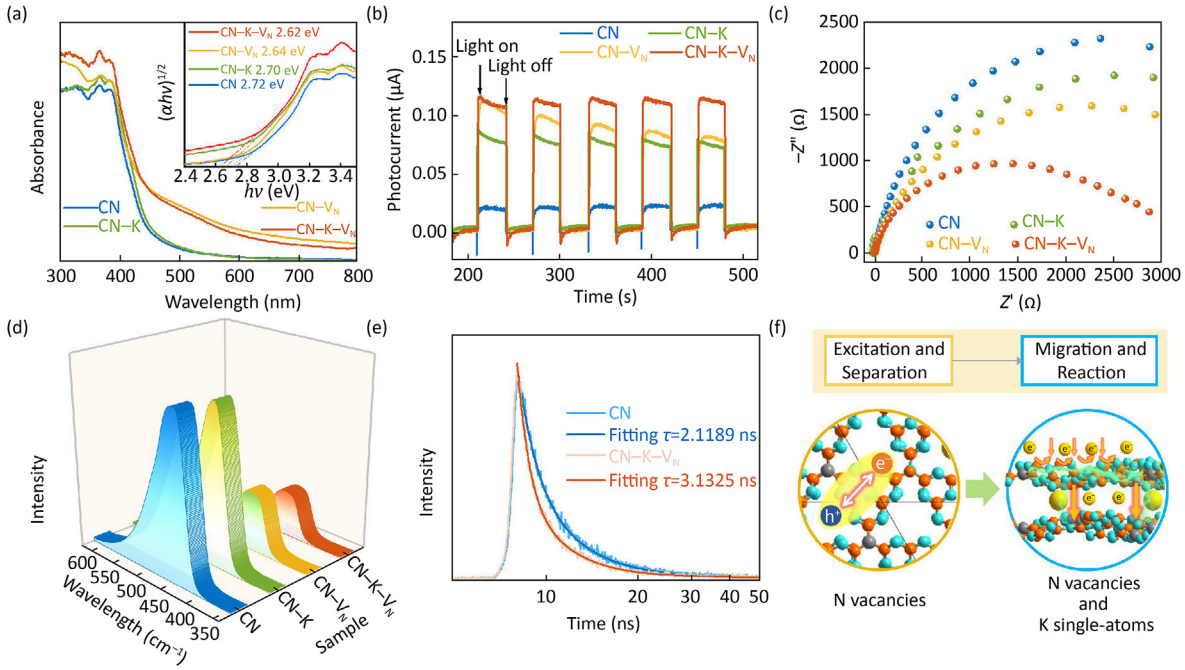

Fig. 4. (a) UV–Vis absorption spectra and the corresponding plots of $(\alpha h\nu)^{1/2}$ *versus* energy ($h\nu$) (inset), (b) PCR measurements, (c) EIS measurements, (d) PL spectra, (e) Time-resolved PL spectra of samples. (f) Schematic illustration of electron separation and migration processes.

transfer resistance (Fig. 4c). The PL spectra show that CN and CN–K exhibit high PL intensity, which diminishes significantly with the introduction of N vacancies, particularly in CN-K-V_N (Fig. 4d). It is well established that lower PL intensity correlates with faster separation and transfer of photogenerated carriers. Thus, these results suggest that CN-K-V_N has a stronger capability of separating and transferring photogenerated e^-/h^+ pairs. This enhancement is attributed to the presence of N vacancies within the plane and K single-atoms in the interlayer of CN, which facilitate both interlayer and intralayer charge transfer, ultimately improving the efficiency of carrier separation and migration. Further analysis using transient fluorescence measurements reveals that the average carrier lifetime of CN-K-V_N is 3.11 ns, surpassing that of CN at 2.13 ns (Fig. 4e). This indicates that the photogenerated e^-/h^+ pairs in CN-K-V_N are effectively separated, or that recombination of these e^-/h^+ pairs is significantly suppressed. Collectively, as illustrated in Fig. 4f, N vacancies within the plane of the CN-K-V_N disrupts the symmetry of C_3N_4, accelerating the excitation and separation of electron-hole pairs. Subsequently, the N vacancies in-plane and K single atoms within layers act as bridges for electron transfer along in-plane and interlayer pathways in C_3N_4, further promoting the migration of electron and hole, which then reaches the interface to participates in the photocatalytic reaction.

3.4. Photocatalytic performance analysis

The photocatalytic performances of the materials were assessed through the degradation of TC under visible light illumination ($\lambda \geq 420$ nm). As shown in Fig. 5a, all the samples can reach adsorption-desorption equilibrium within 20 min, with an adsorption amount of around 5% for TC. Notably, the photocatalytic activity of CN is significantly enhanced by the introduction of N vacancies and the doping of K atoms, particularly for the co-modified CN-K-V_N, which demonstrates the highest activity. Specifically, the CN-K-V_N achieves a TC degradation efficiency of 80.2% within just 10 min of illumination, corresponding to a rate constant of 0.097 min^{-1}, which is 2.6 times greater than that of CN, which has a rate constant of 0.037 min^{-1} (Fig. 5b). CN-K-V_N exhibits a significantly enhanced photocatalytic degradation rate constant for TC following the normalization of K content, suggesting that the single-atom state of K, rather than its concentration, is the primary factor contributing to the observed improvement in photocatalytic performance (Table S4). This enhanced performance can be attributed to the superior surface basicity and superior photoelectronic properties of CN-K-V_N, which facilitates the adsorption of TC substrates and the efficient generation and separation of electrons, as previously demonstrated. Additionally, CN-K-V_N maintains stable and effective photocatalytic degradation activity across a range of TC concentrations (10–40 mol/L), as shown in Fig. S7. As reported in the literature, cyclic experiments are used to investigate the stability of the catalyst [38,39]. The results showed that CN-K-V_N exhibits excellent cyclic stability over at least six cycles, without structural degradation and K loss (Fig. 5c and Fig. S8, Table S3). Furthermore, the remarkable degradation activity of CN-K-V_N extends to various antibiotics, including sulfathiazole and ciprofloxacin, highlighting its broad-spectrum effectiveness (Fig. 5d).

The applicability of this remediation system under real environmental conditions is further evaluated. Specifically, we examine the resistance of CN-K-V_N to various ions present in a simulated water environment. The results indicate that the photocatalytic degradation efficiency of the target pollutant (TC) remains stable (Fig. 5e and Fig. S9), demonstrating the exceptional poison-resistance capability of CN-K-V_N for practical applications. To evaluate the environmental feasibility, we utilized real water samples from Tangxun Lake, the largest urban lake in Wuhan, along with tap water, without any prior treatment, in the photocatalytic degradation process. As shown in Fig. 5f, while the adsorption capacity of CN-K-V_N for TC significantly increases in complex aqueous environments, there is only a negligible decrease in degradation activity. Furthermore, the material achieves an impressive 80% TC conversion within a 20-min illumination period, demonstrating the potential application of CN-K-V_N for antibiotic treatment in natural ecosystems.

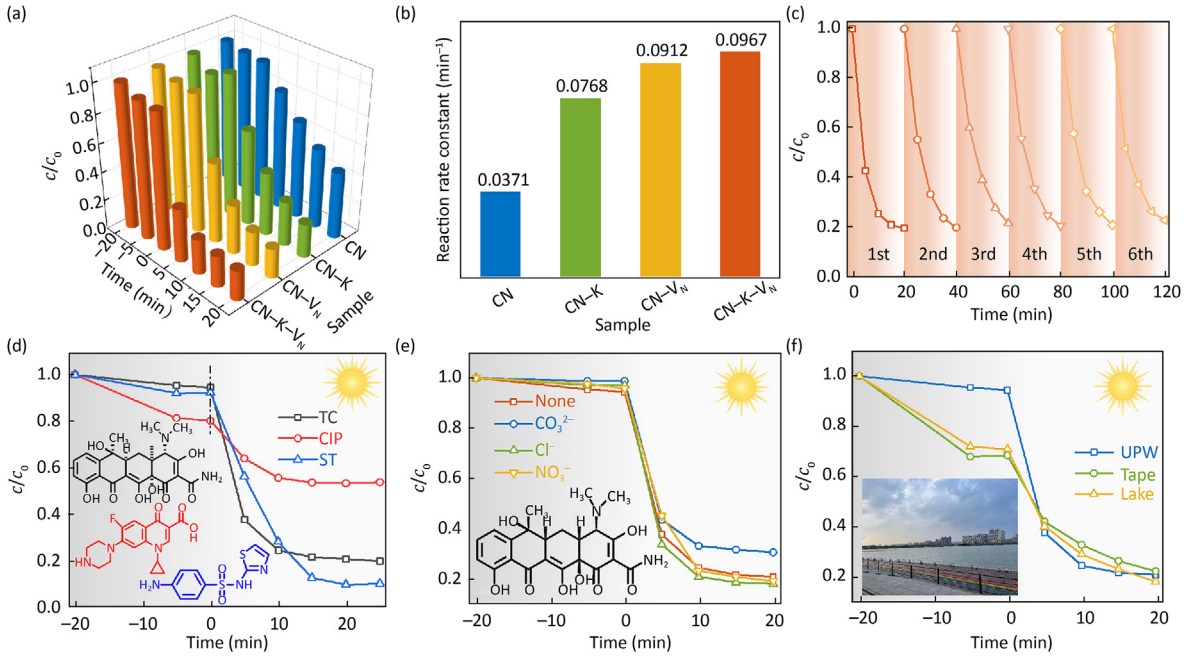

Fig. 5. (a) Photocatalytic degradation of TC and (b) the corresponding degradation rate constants for the samples; (c) Cycling stability of CN-K-V_N during photocatalytic degradation, (d) Degradation activity of CN-K-V_N for different pollutants, (e) Performance under anionic coexistence conditions; (f) Comparison of degradation efficiency in deionized water, tap water and lake water environments.

3.5. *Photocatalytic degradation mechanism of TC*

To identify the reactive species involved in the reaction, we perform trapping experiments and EPR tests. Fig. 6a and Fig. S10 illustrate that the photocatalytic activity of CN-K-V_N is significantly inhibited in the presence of triethanolamine (TEOA) and benzoquinone (BQ), which are used to trap holes and superoxide radicals, respectively. Conversely, the addition of isopropanol (IPA) and β-carotene, which are used to trap hydroxyl radicals and singlet oxygen, has a rather minor effect on the reaction. This indicates that holes and superoxide radicals are the primary reactive species driving the photocatalytic process. To determine the generation of hydroxyl radicals, superoxide radicals and singlet oxygen during the reaction, we conduct EPR measurements. Fig. 6b displays the

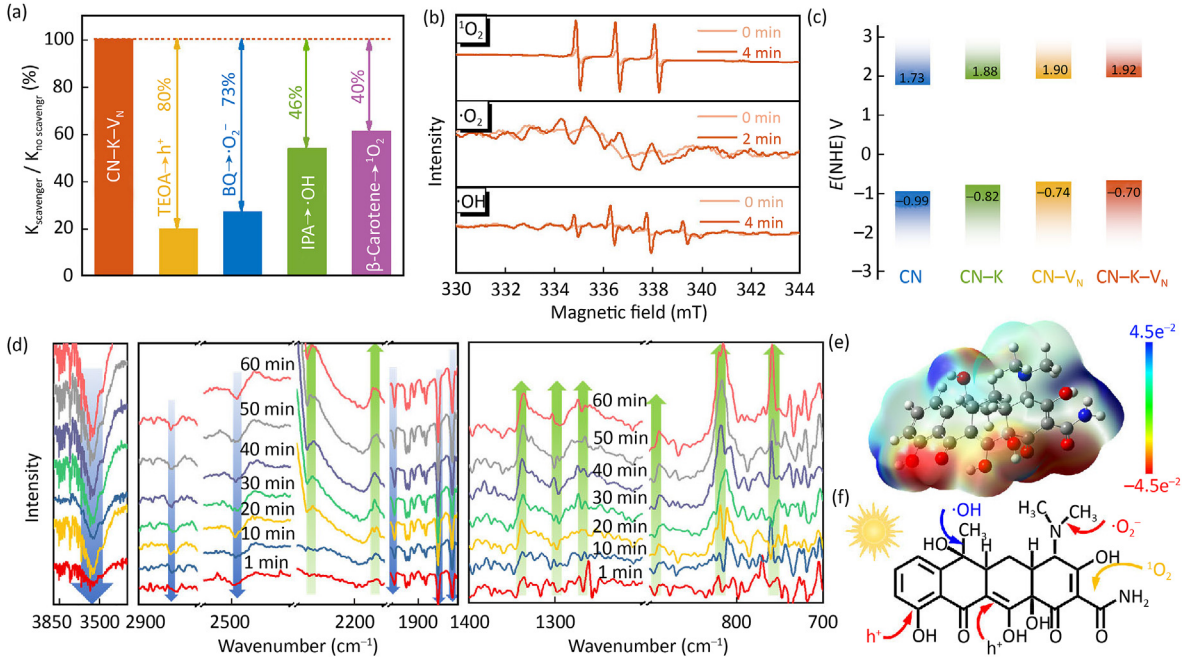

Fig. 6. (a) Photodegradation rates of TC using various scavengers under visible light irradiation for CN-K-V_N; (b) EPR spin-trapping signals indicating the presence of hydroxyl radicals, superoxide radicals and singlet oxygen in the CN-K-V_N system; (c) Band gap measurements of the samples; (d) *In-situ* DRIFTS spectra illustrating the degradation of TC on CN-K-V_N; (e) Electrostatic potential mapping of TC; (f) Schematic representation of the photocatalytic degradation mechanism of TC.

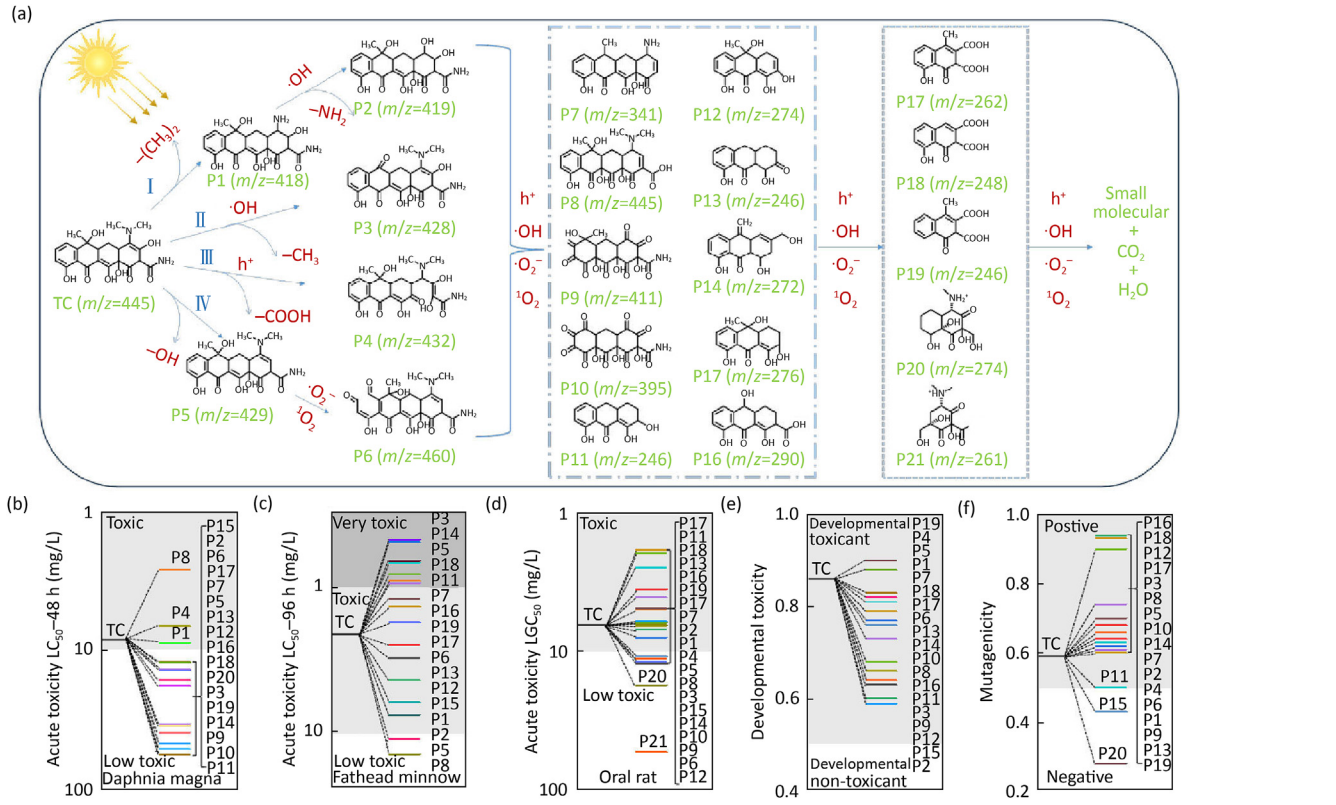

Fig. 7. (a) Proposed degradation pathways of TC over CN-K-V_N under visible light irradiation; (b) LC50 values for daphnia magna (48 h), (c) LC50 values for fathead minnow (96 h), (d) IGC50 values for oral rats, (e) Developmental toxicity, and (f) mutagenicity of TC and its degradation intermediates.

characteristic signals corresponding to TEMP and singlet oxygen adducts, as well as DMPO adducts with superoxide and hydroxyl radicals within the CN-K-V_N photocatalytic system. These findings confirm that hydroxyl radicals, superoxide radicals and singlet oxygen are produced under light irradiation.

To elucidate the mechanism behind the generation of reactive species, we investigated the band gaps of the samples. As shown in Fig. 4a, the band gap gradually narrows with the introduction of N vacancies and the doping of K single-atoms, decreasing from 2.72 eV for CN to 2.62 eV for CN-K-V_N. This narrowing indicates an enhancement of electron excitation. Using X-ray photoelectron spectroscopy (XPS) valence band (VB) measurements and Mott-Schottky analyses (Fig. S11), we estimated the bandgaps of the samples (Fig. 6c). The corresponding data are summarized in Table S5. In the order of CN-K-V_N, CN-V_N, CN–K, CN, the conduction band of sample successively shifts downwards, while the valence band successively shifts upwards. This is attributed to the altered electronic structure by K incorporation and defect energy levels caused by N vacancies [40]. Notably, the VB of CN-K-V_N is measured at 1.92 V, which is higher than that of the other samples. This suggests that the photogenerated holes exhibit stronger oxidation capabilities, thus promoting the oxidative degradation of pollutants. Although its reduction potential is slightly decreased to −0.70 V, this value still enables the effective generation of superoxide radicals through the single-electron reduction of oxygen [41]. Additionally, the O_2-TPD analysis reveals that CN-K-V_N exhibits a significantly stronger O_2 desorption peak associated with chemisorbed O_2, appearing at 115 °C, compared to CN, which shows a peak at 135 °C (Fig. S12). This notable difference highlights the essential roles of N vacancies and K single-atoms in enhancing O_2 adsorption. The production of singlet oxygen is facilitated by hole-mediated oxidation of superoxide radicals, while hydroxyl radicals are generated through the oxidation of free hydroxyl groups [8].

In-situ DRIFTS experiments were conducted to dynamically identify the reaction intermediates and elucidate the potential photodegradation pathways. In the *in-situ* DRIFTS spectra, negative bands indicate the depletion of reactants, while positive bands signify the accumulation of products during the reaction. As shown in Fig. 6d, both negative and positive peaks are present. Notably, the sharp negative bands observed at 3526–3612 cm^{-1} correspond to the stretching vibrations of consumed alcohols and phenols, suggesting that the carbon skeleton of TC is being attacked and decomposed under visible light irradiation. The negative peaks in the range of 1844–1945 cm^{-1}, which are associated with the vibrations of the skeletal structure of TC, indicate the ongoing degradation of the carbon framework of TC over CK-K-V_N during illumination. Concurrently, the pronounced increase in positive bands corresponding to C–H bonds (1273–1338 cm^{-1}) and –COOH groups (817–887 cm^{-1}) signifies the extensive degradation of TC into carboxylic acids and aromatic hydrocarbons. Additionally, electrostatic potential (ESP) mapping indicates that the regions containing alcohols and phenols tend to interact with the negatively charged surface of TC (Fig. 6e). This interaction facilitates the adsorption of TC onto CN-K-V_N, enhancing the reaction efficiency. Based on this evidence, we propose a mechanism for the photocatalytic degradation of TC mediated by reactive species, such as holes and superoxide radicals (Fig. 6f). This mechanism illustrates the conversion of TC into smaller molecules through pathways of demethylation, carboxylation and benzene ring decomposition.

3.6. Photocatalytic degradation pathway of TC and toxicity assessment of products

The LC-MS technique was also applied to analyze the

degradation of TC over various time intervals, enabling the identification of several degradation intermediates. Based on the reaction mechanism, we propose potential photocatalytic degradation pathways for TC, as illustrated in Fig. 7a. The primary degradation process of TC involves four main pathways. In pathway I, the N-methyl groups of TC are progressively removed through the action of holes and reactive oxygen species, resulting in the formation of the P1 intermediate. This is subsequently followed by a hydroxylated deamination process that produces P2. Pathway II closely resembles Pathway I, where TC undergoes demethylation upon attack by hydroxyl radicals (·OH), followed by rapid dehydration and condensation to form the P3 intermediate. In both pathways, the four benzene rings of TC remain intact, and the resulting products primarily arise from the substitution of functional groups within the TC molecule. Pathway III initiates with ring-opening and decarboxylation reactions, yielding the P4 intermediate. Pathway IV involves the removal of a hydroxyl group to produce P5, which is subsequently degraded by reactive oxygen species, leading to formation of P6. As the reaction progresses, TC experiences ring opening, hydroxylation and other transformations induced by reactive species, further disrupting its structure and yielding intermediate molecules within the mass range of $246<m/z<445$ (P7–P16). With ongoing reaction, smaller intermediates, such as P17–P21, are gradually generated. The formation of these intermediates signifies significant damage and effective degradation of the TC structure. Ultimately, all intermediates are oxidized into some smaller molecules and completely decomposed into CO_2 and H_2O.

The biotoxicity of TC and its degradation intermediates was assessed using the Toxicity Estimation Software Tool based on a quantitative structure activity relationship (QSAR) analysis. The results are summarized in Table S6. The LC50 of TC for *Daphnia magna* is 8.37 mg/L, classifying it as 'toxic'. In contrast, the LC50 of the intermediates (excluding P1, P4 and P8) is significantly lower, indicating that the toxic TC is transformed into low-toxicity intermediates (Fig. 7b). However, several intermediates (P3, P14, P5, P18, P11, P7, and P16) exhibit high toxicity to fathead minnows (*Pimephales promelas*), primarily due to the presence of a shared benzene ring (Fig. 7c). In contrast to the primary intermediates (P1–P4), the toxicity of P5 and P6 to oral rats is significantly reduced (Fig. 7d), suggesting that pathway IV is an effective route for mitigating toxicity in mammalian organisms. Despite the formation of some highly toxic intermediates, they are progressively converted into less toxic intermediates (P20, P21) as the reaction continues. Fig. 7e illustrates that the toxicity values of most intermediates have significantly decreased, with the exceptions of P4 and P19. As shown in Fig. 7f, TC is classified as 'mutagenicity positive', while the mutagenicity values for both P15 and P20 are reduced to 'mutagenicity negative'. Overall, the toxicity prediction results indicate that, although some intermediates maintain their harmful effects, extending the reaction time can significantly reduce the overall toxicity.

4. Conclusions

In summary, the dual-site engineering of N vacancies and K single-atoms modifications in C_3N_4 was successfully achieved through a polycondensation route. This process facilitates the formation of N vacancies within the plane and K single-atom sites intercalated between the layers. The N vacancies enhance intraplane charge transfer, while the K single-atom sites improve electron transfer between layers by forming N–K–N bridges, thereby establishing an efficient system for spatial charge separation and migration. Moreover, this dual-site engineering strategy enhances light absorption and optimizes the activation of oxygen. The CN-K-V_N exhibits remarkable photocatalytic efficiency in degrading various organic pollutants, achieving a reaction rate constant of 9.67×10^{-2} min^{-1} for TC degradation. The process of TC degradation involves hydroxylation, demethylation and deamination, followed by further ring-opening and mineralization. Most intermediates exhibit significantly reduced toxicity, highlighting the effectiveness of the degradation process. Notably, degradation experiments conducted in complex water bodies reveal that CN-K-V_N has excellent resistance to interference during pollutant degradation, enhancing its potential for practical applications. The dual-site engineering approach, which synthesizes N vacancies and K single-atom sites in CN-K-V_N, represents a promising strategy for developing effective multifunctional photocatalysts aimed at environmental remediation.

CRediT authorship contribution statement

Xiao Xu: Writing – review & editing, Writing – original draft, Visualization, Funding acquisition, Formal analysis, Data curation, Conceptualization. **Yao Xiao:** Writing – original draft, Investigation, Data curation, Conceptualization. **Xuelian Xu:** Validation, Software, Methodology, Investigation. **Sónia A.C. Carabineiro:** Writing – review & editing, Resources, Funding acquisition, Formal analysis. **Junjiang Zhu:** Writing – review & editing, Supervision, Project administration, Funding acquisition, Formal analysis.

Declaration of competing interest

The authors declare that they have no known competing financial interests or personal relationships that could have appeared to influence the work reported in this paper.

Acknowledgment

This work was financially supported by the National Natural Science Foundation of China (42277485, 21976141), the Department of Science and Technology of Hubei Province (2021CFA034), the Knowledge Innovation Program of Wuhan–Shuguang Project (No. 2023020201020369). SACC acknowledges FCT/MCTES (Fundação para a Ciência e Tecnologia and Ministério da Ciência, Tecnologia e Ensino Superior) for project DOIs: 10.54499/LA/P/0008/2020, 10.54499/UIDP/50006/2020, 10.54499/UIDB/50006/2020 from LAQV and for the Scientific Employment Stimulus - Institutional Call (DOI 10.54499/CEECINST/00102/2018/CP1567/CT0026). We thank the Analytical and Testing Center of Wuhan Textile University for LC-MS test.

Appendix A. Supplementary data

Supplementary data to this article can be found online at https://doi.org/10.1016/j.jmat.2024.100969.

References

[1] Zhu ZP, Zhang XM, Dong HM, Wang ST, Reis S, Li Y, et al. Integrated livestock sector nitrogen pollution abatement measures could generate net benefits for human and ecosystem health in China. Nature Food 2022;3:161–8.
[2] Qin HJ, Zhang WJ, Zheng QL, Zhang PH, Zhang SW, Xu XJ. Design of cobalt-based catalysts with the uniformly distributed core-shell structure for ultra-efficient activation of peroxymonosulfate for tetracycline degradation. J Materiomics 2023;9:882–91.
[3] Sun JJ, Wu HZ, Fu CH, Zhang CH, Hu ZZ, Zhou MH. Novel Fenton-like system based on bifunctional MgO/g-C_3N_4 S-scheme heterojunction photoanode for efficient tetracycline degradation. Appl Catal B Environ Energy 2024;351:123976.
[4] Qi X, Xiong JQ, Zhao CY, Ru SG. Unraveling the key driving factors involved in cometabolism enhanced aerobic degradation of tetracycline in wastewater. Water Res 2022;226:119285.

[5] Yang JY, Liu DL, Li YS, Yang XJ, Liu Y. Radiation construction and excellent performances of Ag NPs/TiO_2/PEG/PVP multifunctional aerogel: adsorption-photocatalytic degradation, photosensitive antibacterial and cytotoxicity. J Materiomics 2024;10:585–93.
[6] Luo X, Zhao LX, Zhou HJ, He L, Lei X, Guan QQ, et al. Oxygen vacancy induction strategy to regulate the evolution of valence- and free-electrons for boosting visible photodegradation of tetracycline hydrochloride. J Hazard Mater 2024;466:133624.
[7] Cao GQ, Shen ZR, Cui JS, Yu MY, Li WZ. Bifunctional activation of peroxymonosulfate over CuS/g-C_3N_4 composite for efficient degradation of tetracycline antibiotics. Chem Eng J 2024;483:149082.
[8] Wang M, Lu GH, Jiang RR, Dang TJ, Chen YF, Liu JC, et al. Carbon vacancies and spatial confinement effects of V_C-$FCN_{0.3}$ prepared by spatial self-corrosion strategy achieved eco-friendly photocatalytic degradation to bisphenol F. J Clean Prod 2024;447:141545.
[9] Zhang SJ, Zheng HC, Tratnyek PG. Advanced redox processes for sustainable water treatment. Nature Water 2023;1:666–81.
[10] Xu X, Ding X, Yang X, Wang P, Li S, Lu ZX, et al. Oxygen vacancy boosted photocatalytic decomposition of ciprofloxacin over Bi_2MoO_6: oxygen vacancy engineering, biotoxicity evaluation and mechanism study. J Hazard Mater 2019;364:691–9.
[11] Zhang HB, Wang ZL, Zhang JF, Dai K. Metal-sulfide-based heterojunction photocatalysts: principles, impact, applications, and *in-situ* characterization. Chin J Catal 2023;49:42–67.
[12] Xu XT, Zhang JF, Wang ZL, Dai K. Rational design of S-scheme CeO_2/Bi_2MoO_6 microsphere heterojunction for efficient photocatalytic CO_2 reduction. Acta Phys Chim Sin 2024;40:2309031.
[13] Dharmarajan NP, Vidyasagar D, Yang JH, Talapaneni SN, Lee J, Ramadass K, et al. Bio-inspired supramolecular self-assembled carbon nitride nanostructures for photocatalytic water splitting. Adv Mater 2023;36:2306895.
[14] Guan KK, Li JY, Lei W, Wang HH, Tong ZM, Jia QL, et al. Synthesis of sulfur doped g-C_3N_4 with enhanced photocatalytic activity in molten salt. J Materiomics 2021;7:1131–42.
[15] Lin H, Xiao Y, Geng AX, Bi HT, Xu X, Xu XL, et al. Research progress on graphitic carbon nitride/metal oxide composites: synthesis and photocatalytic applications. Int J Mol Sci 2022;23:12979.
[16] Chen DD, Wang ZL, Fu JW, Zhang JF, Dai K. Ethyl-activated carbon nitride for efficient photocatalytic CO_2 conversion. Sci China Mater 2024;67:541–9.
[17] He HW, Wang ZL, Zhang JF, Shao CF, Dai K, Fan K. Interface chemical bond enhanced ions intercalated carbon nitride/CdSe-diethylenetriamine S-scheme heterojunction for photocatalytic H_2O_2 synthesis in pure water. Adv Funct Mater 2024;34:2315426.
[18] Yu MX, Chang SX, Ma L, Wu XF, Yan JT, Ding YB, et al. Remarkable improvement in photocatalytic activity of g-C_3N_4 for NO oxidation through surface hydroxylation. Sep Purif Technol 2024;354:128695.
[19] Wang J, Wang ZL, Zhang JF, Dai K. Single-layer crystalline triazine-based organic framework photocatalysts with different linking groups for H_2O_2 production. Chin J Struct Chem 2023;42:100202.
[20] Guo YF, Li J, Yuan YP, Li L, Zhang MY, Zhou CY, et al. A rapid microwave-assisted thermolysis route to highly crystalline carbon nitrides for efficient hydrogen generation. Angew Chem Int Ed 2016;55:14693–7.
[21] Cai X, Li Y, Zhang YF, Lin W. π–π interaction-driven charge separation and interlayer transfer in polymeric carbon nitride. ACS Catal 2023;13:15877–85.
[22] Xiao XD, Gao YT, Zhang LP, Zhang JC, Zhang Q, Li Q, et al. A promoted charge separation/transfer system from Cu single atoms and C_3N_4 layers for efficient photocatalysis. Adv Mater 2020;32:2003082.
[23] Li H, Cheng B, Xu JS, Yu JG, Cao SW. Crystalline carbon nitrides for photocatalysis. EES Catal 2024;2:411–47.
[24] Hu XL, Zhang Z, Lu P, Zhou YH, Zhou YY, Bai Y, et al. Cyano-deficient g-C_3N_4 for round-the-clock photocatalytic degradation of tetracycline: mechanism and application prospect evaluation. Water Res 2024;260:121936.
[25] Ye QJ, Zhou YM, Xu YY, Zhang Q, Shi XL, Li D, et al. Improved charge transfer in polymeric carbon nitride synergistically induced by the aromatic rings modification and Schottky junctions for efficient photocatalytic CO_2 reduction. Chem Eng J 2023;463:142395.
[26] Zhang Y, Cao N, Liu XM, He FT, Zheng B, Zhao CC, et al. Enhanced electron density of the π-conjugated structure and in-plane charge transport to boost photocatalytic H_2 evolution of g-C_3N_4. Sci China Mater 2023;66:2274–82.
[27] Zhang GQ, Zhu JY, Xu YS, Yang C, He CX, Zhang PX, et al. In-plane charge transport dominates the overall charge separation and photocatalytic activity in crystalline carbon nitride. ACS Catal 2022;12:4648–58.
[28] Kumar P, Singh G, Guan X, Lee J, Bahadur R, Ramadass K, et al. Multifunctional carbon nitride nanoarchitectures for catalysis. Chem Soc Rev 2023;52:7602–64.
[29] Zhang ZZ, Sun QM, Ji R, Chen DY, Li NJ, Li H, et al. Boosted photogenerated charge carrier separation by synergy of oxygen and phosphorus co-doping of graphitic carbon nitride for efficient 2-chlorophenol photocatalytic degradation. Chem Eng J 2023;471:144388.
[30] Shen JC, Luo CH, Qiao SS, Chen YQ, Tang YH, Xu JQ, et al. Single-atom Cu channel and n-vacancy engineering enables efficient charge separation and transfer between C_3N_4 interlayers for boosting photocatalytic hydrogen production. ACS Catal 2023;13:6280–8.
[31] Xiong T, Cen WL, Zhang YX, Dong F. Bridging the g-C_3N_4 Interlayers for enhanced photocatalysis. ACS Catal 2016;6:2462–72.
[32] Xu KJ, Cui KP, Cui MS, Liu XY, Chen X. Carbonyl heterocycle modified mesoporous carbon nitride in photocatalytic peroxydisulfate activation for enhanced ciprofloxacin removal: performance and mechanism. J Hazard Mater 2023;444:130412.
[33] Zhao S, Liu YP, Wang YY, Fang JS, Qi YQ, Zhou YM, et al. A self-assembly strategy to synthesize carbon doped carbon nitride microtubes with a large π-electron conjugated system for efficient H_2 evolution. Chem Eng J 2022;447:137436.
[34] Zhou Y, Jiang DN, Wang ZW, Yi LD, Sun JX, Liu DL, et al. Bandgap engineering of carbon nitride by formic acid assisted thermal treatment for photocatalytic degradation of tetracycline hydrochloride. Chem Eng J 2024;485:149830.
[35] Jin XL, Wang HQ, Lv XT, Lan Q, Ge T, Guo L, et al. K–N bridge-mediated charge separation in hollow g-C_3N_4 frameworks: a bifunctional photocatalysts towards efficient H_2 and H_2O_2 production. J Colloid Interface Sci 2023;652:1545–53.
[36] Li YH, Shi L, Mao Y, Zhang Y, Wang HQ. Efficient reduction of uranyl under aerobic conditions by sodium and potassium co-doped carbon nitride. Chem Eng J 2022;446:136872.
[37] Zhao S, Liu YP, Wang YY, Fang JS, Qi YQ, Zhou YM, et al. Carbon and phosphorus co-doped carbon nitride hollow tube for improved photocatalytic hydrogen evolution. J Colloid Interface Sci 2022;616:152–62.
[38] He HW, Wang ZL, Dai K, Li SW, Zhang JF. LSPR-enhanced carbon-coated In_2O_3/$W_{18}O_{49}$ S-scheme heterojunction for efficient CO_2 photoreduction. Chin J Catal 2023;48:267–78.
[39] Yang TT, Wang J, Wang ZL, Zhang JF, Dai K. Ipolymer $Cd_3(C_3N_3S_3)_2$/$Zn_3(C_3N_3S_3)_2$ S-scheme heterojunction enhances photocatalytic H_2 production. Chin J Catal 2024;58:157–67.
[40] Wu XH, Tan LH, Chen GQ, Kang JY, Wang GH. g-C_3N_4-based S-scheme heterojunction photocatalysts. Sci China Mater 2024;67:444–72.
[41] Hao RR, Wang GH, Tang H, Sun LL, Xu C, Han DY. Template-free preparation of macro/mesoporous g-C_3N_4/TiO_2 heterojunction photocatalysts with enhanced visible light photocatalytic activity. Appl Catal B Environ 2016;187:47–58.

Xiao Xu received his Ph.D. degree at Huazhong Agricultural University in 2022. Now, he is a lecturer of College of Chemistry and Chemical Engineering at Wuhan Textile University. His research interests focus on the photocatalytic environmental purification and photochemical regulation of reactive oxygen species.

Yao Xiao received her Master degree from Wuhan Textile University in 2024. Her research interests focus on the design and synthesis of g-C_3N_4-based photocatalysts for environmental applications.

Junjiang Zhu received his Ph.D. degree in Physical Chemistry in 2005 from Changchun Institute of Applied Chemistry, CAS. He is a professor of the College of Chemistry and Chemical Engineering of Wuhan Textile University, and currently is the Chutian Distinguished Professor of Hubei Province. His research interest focuses on environmental catalysis (Removal of NO_x, CO and VOCs), green synthesis (selective oxidation/hydrogenation) and functional materials (graphitic carbon nitride, perovskite oxides, *etc.*). He has charged 11 research projects, published ~80 scientific papers and 5 patents as the first or corresponding author. He has won the Natural Science Award of Hubei province in 2023 (the second prize).